

DoD and DoA Estimation Method for Sparse MIMO Radar in Multipath Environment

Haolan Luo^{ID}, *Student Member, IEEE*, Wenqiang Wei^{ID}, Meiqiu Jiang^{ID}, *Graduate Student Member, IEEE*, Jinghui Zhu^{ID}, Shisheng Guo^{ID}, *Senior Member, IEEE*, Tong Gan^{ID}, and Guolong Cui^{ID}, *Senior Member, IEEE*

Abstract—To achieve high angular resolution with a small physical aperture, multiple input multiple output (MIMO) equivalent virtual array technology is frequently used to expand antenna aperture, typically with a sparse transmitting array. However, in multipath environments, using virtual aperture techniques to independently estimate the direction of departure (DoD) and direction of arrival (DoA) of multipath signals with unequal DoD and DoA is inaccurate. Additionally, joint estimation of the DoD and DoA of signals requires simultaneous searching in both DoD and DoA dimensions, leading to significant computational overhead. Furthermore, sparse transmitting arrays introduce grating lobes in the DoD dimension, complicating accurate estimation of the DoD of signals. To address these challenges, this article proposes a joint estimation method for DoD and DoA in multipath environments using sparse MIMO radar. This method first estimates the DoA of signals to design a spatial filter that suppresses the grating lobes in the DoD spectrum. Subsequently, joint estimation of DoD and DoA is conducted, enabling rapid and accurate estimation of signal DoD and DoA. Finally, simulation and experimental data validate the accuracy and effectiveness of the proposed approach.

Index Terms—Direction of arrival (DoA), direction of departure (DoD), grating lobes, multipath, operating efficiency, sparse multiple input multiple output (MIMO).

I. INTRODUCTION

RADARS offer the advantage of all-weather, all-day operation and have been widely applied in automotive radar systems in recent years [1]. However, the characteristics of

Received 27 August 2025; revised 9 December 2025; accepted 27 December 2025. Date of publication 23 January 2026; date of current version 6 February 2026. This work was supported in part by the Postdoctoral Science Foundation of Sichuan Province under Grant TB2025086, in part by the Science Foundation of Tianfu Jiangxi Laboratory under Grant 2025013, in part by the National Natural Science Foundation of China under Grant 62371110, and in part by the Natural Science Foundation of Sichuan Province under Grant 2025ZNSFSC0467. The Associate Editor coordinating the review process was Dr. Michael Gadringer. (*Corresponding author: Shisheng Guo*.)

Haolan Luo, Shisheng Guo, and Guolong Cui are with the Tianfu Jiangxi Laboratory, Chengdu 641419, China, and also with the School of Information and Communication Engineering, University of Electronic Science and Technology of China, Chengdu 611731, China (e-mail: luohaolan@jxl.ac.cn; ssquo@uestc.edu.cn; cuiguolong@uestc.edu.cn).

Wenqiang Wei and Meiqiu Jiang are with the School of Information and Communication Engineering, University of Electronic Science and Technology of China, Chengdu 611731, China (e-mail: Wenqiangwei@std.uestc.edu.cn; mqjiang@std.uestc.edu.cn).

Jinghui Zhu is with the Academy of Broadcasting Science, NRTA, Beijing 100866, China (e-mail: zhujinghui@abs.ac.cn).

Tong Gan is with the Tianfu Jiangxi Laboratory, Chengdu 641419, China (e-mail: gantong2005@163.com).

Digital Object Identifier 10.1109/TIM.2026.3657561

multipath propagation of electromagnetic (EM) waves result in the presence of multipath ghost signals in the echo signal, in addition to containing the effective information of the real target. Multipath signals can increase the false alarm probability, posing significant challenges for the application of automotive radar.

Currently, the processing of multipath signals can be broadly categorized into suppression and utilization methods. Regarding the suppression of multipath signals, the main methods include synthetic aperture radar (SAR) imaging techniques [2], neural networks [3], generalized likelihood ratio methods [4], and antenna design approaches [5], among others. However, in automotive radar systems, multipath signals can sometimes be beneficial for target detection. When the line-of-sight (LOS) of the driver is obstructed by objects such as buildings at street corners, utilizing the reflective signal from opposite buildings [6], [7] can expand the detection field of view of EM waves, enabling non-LOS (NLOS) target detection and ensuring driving safety. Therefore, investigating methods for utilizing multipath signals is of great significance for ensuring safe driving.

Before multipath utilization, accurate identification of LOS signals and multipath signals is essential. A common method for identifying multipath signals is through data fusion from multiple sensors [8]. Although this method achieves high accuracy, it requires additional sensors as auxiliary means. Another prevalent approach is the use of machine learning and deep learning methods for identifying multipath signals [9], [10], [11], [12]. However, these methods require large datasets for training and cannot guarantee the stability of identification results when the testing environment changes.

Unlike the aforementioned methods, Feng et al. [13] proposed a method for identifying multipath signals based on the range-Doppler relationship of multipath signals. However, this method requires sufficient signal-to-noise ratio (SNR) for LOS path, first-order multipath, and second-order multipath signals to ensure that they can be detected. In fact, the energy of EM waves significantly attenuates after reflection, so it cannot always be guaranteed that various types of multipath signals exist in the echo signals.

Benefiting from the ability of multiple input multiple output (MIMO) arrays to provide large virtual aperture [1], the angular relationships between multipath signals have been used to identify multipath signals. However, this method has an important problem in a multipath environment. A schematic

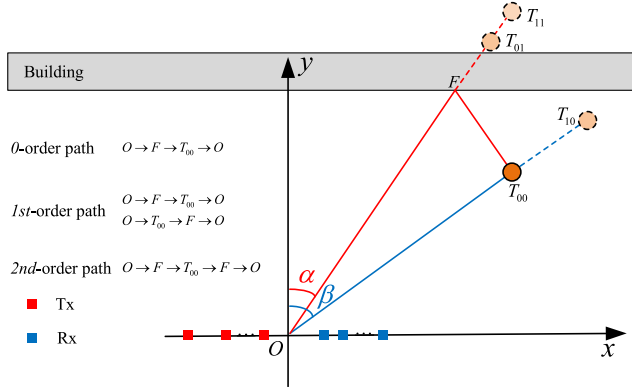


Fig. 1. Multipath propagation geometric model.

of a common multipath scenario is shown in Fig. 1. O , T_{00} , and F represent the positions of the radar, the target, and the EM wave reflection point, respectively. α and β denote, respectively, the direction of departure (DoD) and direction of arrival (DoA) of the propagation path $O \rightarrow F \rightarrow T_{00} \rightarrow O$. As illustrated in Fig. 1, for first-order multipath, there are two propagation paths with opposite directions, denoted as $O \rightarrow F \rightarrow T_{00} \rightarrow O$ and $O \rightarrow T_{00} \rightarrow F \rightarrow O$. Since these two paths differ only in their propagation directions while having identical distances and velocities [13], a multipath coupling phenomenon occurs. This phenomenon leads to the failure of the angle estimation method based on an equivalent virtual array. Consequently, many researchers have addressed this issue by simultaneously performing angular searches across both the DoD and DoA dimensions to obtain accurate angle estimation results [14], [15], [16], [17], [18].

However, most of the time, to achieve a large virtual aperture, the transmitting array of MIMO radar is designed to be sparse. According to the Nyquist sampling theorem, sparse transmission generates grating lobes in the DoD dimension, thereby affecting the judgment of the main lobe position. In [14], [15], and [16], uniformly spaced transmitting antennas are employed, which are not applicable to radars with sparsely distributed transmit arrays. Although the studies in [17] and [18] adopt sparsely distributed transmitting arrays, they do not address the grating lobes in any way.

To achieve joint estimation of DoD and DoA while suppressing the grating lobe issue caused by sparse transmitting array elements, we previously proposed a grating lobe suppression method based on DoD-DoA spectrum characteristics [19]. Although this method effectively suppresses grating lobes, it requires exhaustive angle searches in both DoD and DoA dimensions, consuming significant computational resources. To reduce the computational complexity of the DoD-DoA spectrum, Park et al. [20] first estimate DoA and then estimate DoD, thereby transforming the challenge of 2-D spectrum estimation into a 1-D problem. However, in multipath environments, first-order multipath signals always occur simultaneously and are correlated with each other [21]. If only the receiving antennas are used for DoA estimation, the limited aperture of the receiving antennas will decrease the accuracy of DoA estimation, consequently reducing the accuracy of DoD estimation as well. Moreover, this method

does not address the grating lobe issue in the DoD dimension caused by sparse transmitting array elements. Therefore, there is a current need for a method that can rapidly and accurately achieve DoD and DoA estimation using sparse MIMO arrays in multipath environments.

To address this issue, inspired by [20], we propose a new method for joint estimation of DoD and DoA in sparse MIMO radar systems in multipath environments. Initially, the DoA spectrum of the signal is estimated to design a spatial filter for suppressing the DoD spectrum grating lobes. Then, based on the DoD spectra before and after suppressing the grating lobes, the effective DoD spectrum peak positions are selected. Next, based on the spectral peak position of DoD, all possible combinations of DoD and DoA are traversed to estimate the corresponding power of the DoD-DoA heat map. Furthermore, the combination of DoD and DoA corresponding to the maximum energy is selected from the traversal results as the estimation of DoD and DoA. Finally, the feasibility of the proposed method is validated through simulation and experimental data based on millimeter wave (MMW) radar.

The primary contributions of this article are summarized as follows.

- 1) Leveraging the advantages of high-resolution DoD spectrum and grating lobe-free DoA spectrum in MIMO radars with sparse transmitting arrays, this study proposes a novel signal angle estimation method tailored for multipath environments.
- 2) To address the distortion of the DoD spectrum caused by spatial filtering, this article proposes a DoD effective spectral peak confirmation method based on the monotonicity of the first-order derivative of the DoD spectrum.
- 3) Some experiments with varying target positions, quantities, and test scenarios are carried out to demonstrate the feasibility of the proposed algorithm.

The subsequent chapters of this article are structured as follows. The necessity of joint estimation of DoD and DoA using MIMO radar in multipath environments is demonstrated in Section II, and the proposed method is introduced in detail in Section III. Subsequently, numerical simulations and experiments are conducted and presented in Section IV. Finally, the discussion and conclusion of this article are presented in Section V.

II. PROBLEM FORMULATION

To achieve sufficient angular resolution within a limited physical aperture, researchers have devised MIMO radar signal waveforms [22], [23]. A typical time-division MIMO array with M transmitting elements and N receiving elements is illustrated in Fig. 2. In this MIMO array, the distance d_r between adjacent receiving antennas is $\lambda/2$ (λ denotes the signal wavelength, determined by the center frequency of the transmitted signal), and the distance d_t between adjacent transmitting antennas is $N\lambda/2$. Therefore, the distance d between adjacent elements in the equivalent virtual array is $\lambda/2$, and the total length of the virtual aperture is $L = (mn - 1)\lambda/2$. Assuming a target is located at a distance D from the radar,

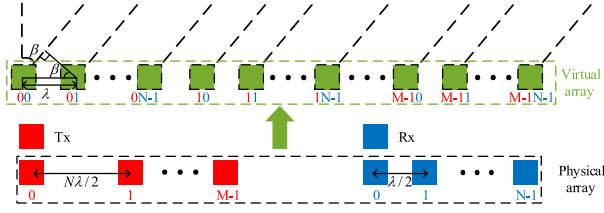


Fig. 2. Diagram illustrating the equivalent virtual array of a classic MIMO array.

forming an angle β with the normal to the virtual array. When D and L satisfy $D > 2L^2/\lambda$, EM waves can be approximated as parallel incidence on a virtual array. In this scenario, the phase difference between adjacent virtual elements is given by

$$\Delta\varphi = \frac{2\pi d \sin\beta}{\lambda}. \quad (1)$$

Taking the virtual element 00 which is depicted in Fig. 2 as the reference element, and disregarding the initial phase of the transmitting signal, the expression for the receiving signal at each virtual element can be expressed as

$$r_{mn}(k) = A_{mn}(k) e^{-j(m+n)\Delta\varphi} \quad (2)$$

where $m \in [0, 1, \dots, M-1]$ and $n \in [0, 1, \dots, N-1]$, and $A_{mn}(k)$ is the amplitude of the echo at the k th sampling point corresponding to the m th transmitting antenna and the n th receiving antenna. Considering that the transmitting signal of MMW radar is frequency modulated continuous wave (FMCW) [24], after mixing, the beat signal can be regarded as a point frequency signal [20], so the expression of $A_{mn}(k)$ is

$$A_{mn}(k) = A_{b,mn} e^{-j2\pi(f_0\tau + \mu\tau k - \mu\tau^2/2)}. \quad (3)$$

Herein, f_0 , τ , μ , and $A_{b,mn}$ represent the carrier frequency of the transmitting signal, the time delay of the receiving signal, the frequency modulation slope, and the amplitude of the beat signal, respectively. Performing the fast Fourier transform (FFT) on $r_{mn}(k)$, the corresponding signal expression at time delay τ for each channel is

$$R_{mn}(\tau) = A_F(\tau) e^{-j(m+n)\Delta\varphi} \quad (4)$$

where $A_F(\tau)$ is the amplitude at time delay τ .

To simplify the analysis, the signal strength received by different array elements is assumed to be uniform. After performing spatial Fourier transform (SFT) on (4), we obtain

$$\begin{aligned} \mathcal{R}(\varphi) &= \sum_{m=0}^{M-1} \sum_{n=0}^{N-1} R_{mn}(\tau) e^{j(m+n)\varphi} \\ &= A_F(\tau) \sum_{m=0}^{M-1} e^{jm(\varphi-\Delta\varphi)} \sum_{n=0}^{N-1} e^{jN(\varphi-\Delta\varphi)} \\ &= A_F(\tau) \frac{1 - e^{jm(\varphi-\Delta\varphi)}}{1 - e^{j(\varphi-\Delta\varphi)}} \frac{1 - e^{jN(\varphi-\Delta\varphi)}}{1 - e^{j(\varphi-\Delta\varphi)}}. \end{aligned} \quad (5)$$

Let $\varphi - \Delta\varphi = \gamma$, so

$$\begin{aligned} 1 - e^{j\gamma} &= 1 - (\cos\gamma + j\sin\gamma) \\ &= 1 - \left(1 - 2\sin^2\frac{\gamma}{2} + 2j\sin\frac{\gamma}{2}\cos\frac{\gamma}{2}\right) \end{aligned}$$

$$\begin{aligned} &= -2j\sin\frac{\gamma}{2} \left(\cos\frac{\gamma}{2} + j\sin\frac{\gamma}{2}\right) \\ &= -2j\sin\frac{\gamma}{2} e^{j\frac{\gamma}{2}}. \end{aligned} \quad (6)$$

Therefore, (5) can be rewritten as

$$\begin{aligned} \mathcal{R}(\varphi) &= \frac{-2j\sin\left(\frac{M}{2}(\varphi - \Delta\varphi)\right) e^{j\frac{M}{2}(\varphi - \Delta\varphi)}}{-2j\sin\left(\frac{1}{2}(\varphi - \Delta\varphi)\right) e^{j\frac{1}{2}(\varphi - \Delta\varphi)}} \\ &= A_F(\tau) \frac{\sin\left(\frac{M}{2}(\varphi - \Delta\varphi)\right)}{\sin\left(\frac{1}{2}(\varphi - \Delta\varphi)\right)} e^{j\frac{M-1}{2}(\varphi - \Delta\varphi)} \\ &\quad \times \frac{\sin\left(\frac{N}{2}(\varphi - \Delta\varphi)\right)}{\sin\left(\frac{1}{2}(\varphi - \Delta\varphi)\right)} e^{j\frac{N-1}{2}(\varphi - \Delta\varphi)}. \end{aligned} \quad (7)$$

Absolutely, $|\mathcal{R}(\varphi)|^2$ will reach its maximum value when $\varphi = \Delta\varphi$. This process represents the fundamental principle of angle estimation in MIMO arrays.

In fact, only the phase of the signal reflected back to the receiving array from the target is considered in (2) and the phase of the signal left from the transmitting array is ignored. However, in multipath environments, the signal from the target may not only be reflected directly back to the radar but also be reflected off other objects in the environment before returning to the radar. This results in discrepancies between the DoD and DoA of the EM wave.

As illustrated in Fig. 1, in addition to the direct path $O \rightarrow T_{00} \rightarrow O$, there are several other propagation paths caused by reflection surfaces, denoted as $O \rightarrow F \rightarrow T_{00} \rightarrow O$, $O \rightarrow T_{00} \rightarrow F \rightarrow O$ and $O \rightarrow F \rightarrow T_{00} \rightarrow F \rightarrow O$. These paths result in the formation of three multipath ghost targets, T_{10} , T_{01} and T_{11} , which are shown in Fig. 1. For convenience in subsequent descriptions, these four paths are designated as \mathcal{P}_{00} , \mathcal{P}_{10} , \mathcal{P}_{01} , and \mathcal{P}_{11} , respectively. It is worth noting that, when EM waves propagate along paths \mathcal{P}_{00} and \mathcal{P}_{11} , their corresponding DoD and DoA are identical. However, when EM waves propagate along paths \mathcal{P}_{01} and \mathcal{P}_{10} , the DoD and DoA of these two paths are not equal.

In the principle of angle estimation using virtual aperture technology in MIMO arrays, as indicated in (2), the receiving signal model includes only the DoA of the signal and does not account for the DoD. Therefore, this receiving signal model is applicable to the signals propagating along paths \mathcal{P}_{00} and \mathcal{P}_{11} , rather than those propagating along paths \mathcal{P}_{01} and \mathcal{P}_{10} . Accordingly, the signal model for array signals in multipath environments should be

$$R_{mn}(\tau) = A_F(\tau) e^{-j(m\Delta\phi + n\Delta\varphi)} \quad (8)$$

where $\Delta\phi$ and $\Delta\varphi$ represent the phase differences of adjacent transmitting and receiving elements, respectively, and their expressions are

$$\begin{aligned} \Delta\phi &= \frac{2\pi d_t \sin\alpha}{\lambda} \\ \Delta\varphi &= \frac{2\pi d_r \sin\beta}{\lambda}. \end{aligned} \quad (9)$$

Similar to (7), after performing SFT on (8), we have

$$\mathcal{R}(\alpha, \beta) = \sum_{m=0}^{M-1} \sum_{n=0}^{N-1} R_{mn}(\tau) e^{j(m\phi + n\varphi)}$$

$$\begin{aligned}
&= A_F(\tau) \sum_{m=0}^M e^{jm(\phi-\Delta\phi)} \sum_{n=0}^N e^{jN(\varphi-\Delta\varphi)} \\
&= A_F(\tau) \frac{1 - e^{jm(\phi-\Delta\phi)}}{1 - e^{j(\phi-\Delta\phi)}} \frac{1 - e^{jN(\varphi-\Delta\varphi)}}{1 - e^{j(\varphi-\Delta\varphi)}} \\
&= A_F(\tau) \frac{\sin\left(\frac{M}{2}(\phi - \Delta\phi)\right)}{\sin\left(\frac{1}{2}(\phi - \Delta\phi)\right)} e^{j\frac{M-1}{2}(\phi - \Delta\phi)} \\
&\times \frac{\sin\left(\frac{N}{2}(\varphi - \Delta\varphi)\right)}{\sin\left(\frac{1}{2}(\varphi - \Delta\varphi)\right)} e^{j\frac{N-1}{2}(\varphi - \Delta\varphi)}. \quad (10)
\end{aligned}$$

From (10), it is evident that $|\mathcal{R}(\alpha, \beta)|^2$ will reach its maximum value when $\phi = \Delta\phi$ and $\varphi = \Delta\varphi$. Furthermore, a comparison between (5) and (10) reveals that when $\phi = \varphi$, both equations yield identical spectral peak positions. This demonstrates that the two signal models corresponding to (4) and (8) are both applicable for estimating the spectral peak positions of signals with equal DoD and DoA. However, when $\phi \neq \varphi$, (5) is not applicable for estimating the spatial spectrum of signals with unequal DoD and DoA. In a multipath environment, it is difficult to determine which path the signal is propagating through, making it challenging to choose the appropriate signal model from (4) or (8) for acquiring the angle spectrum. Therefore, although the method of equivalent virtual aperture can increase the aperture and improve angular resolution, it is not suitable for DoA estimation in multipath environments. In this case, it is necessary to use the signal model corresponding to (8) to simultaneously estimate the DoD and DoA of the signal.

To validate the above analysis, we conducted simulation experiments. The simulation scenario is illustrated in Fig. 1, using an MIMO array with three transmitting antennas and four receiving antennas. The signal works at a carrier frequency of 77 GHz, with spacing between adjacent transmitting and receiving antennas being 2λ and $\lambda/2$, respectively. The beat signal model is described by (3). Additionally, the receiving signal includes two signals propagating along paths \mathcal{P}_{10} and \mathcal{P}_{01} simultaneously. For path \mathcal{P}_{10} , the DoD and DoA are set to 20° and 5° , respectively, while for path \mathcal{P}_{01} , they are set to 5° and 20° , respectively. The other simulation parameters are shown in Table I.

First, (10) is employed to estimate the DoD and DoA of the beat signal simultaneously, and the result is depicted in Fig. 3(a). It is observed that there are grating lobes in the DoD dimension, which hinders the accurate determination of the DoD.

Subsequently, (5) is used to estimate the DoA based on the equivalent virtual aperture, resulting in the blue spectrum shown in Fig. 3(b). Since the simulation only included signals propagating along paths \mathcal{P}_{01} and \mathcal{P}_{10} , there should theoretically be only two valid spectral peaks in Fig. 3(b). However, in addition to peaks labeled 2 and 3, the blue spectrum also contains peaks labeled 1 and 4.

As discussed above, (5) is essentially a special case of (10). Consequently, extracting data along with the white dashed line in Fig. 3(a) produces the spectrum depicted with red circles in Fig. 3(b). It is evident that this spectrum fully overlaps with the blue spectrum, confirming the accuracy of the analysis related to (5) and (10). Therefore, peaks labeled 1 and 4 in

TABLE I
SIMULATION SIGNAL PARAMETERS

Parameter	Value
Bandwidth	3.5 GHz
Sampling frequency	2 MHz
Frequency slope	35 MHz/us
Range resolution	4.3 cm
PRT	0.1 ms
The number of snapshots	1
SNR of beat signal	10 dB

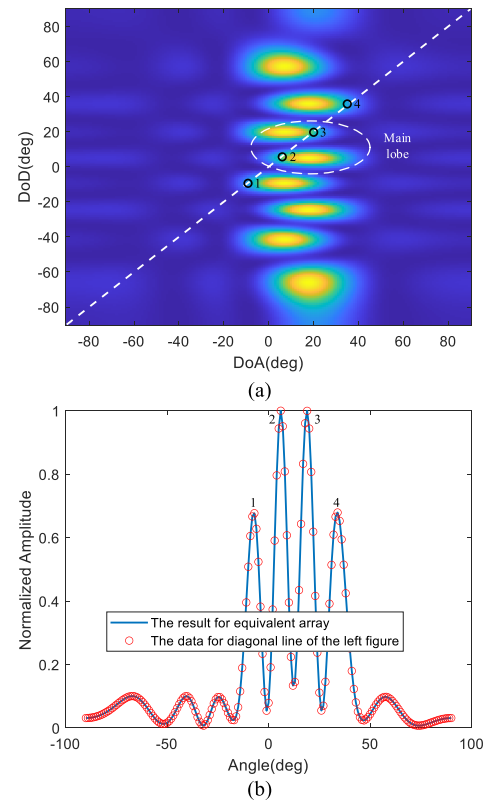


Fig. 3. Angle spectra of paths \mathcal{P}_{01} and \mathcal{P}_{10} . (a) 2-D DoD-DoA angle spectrum and (b) 1-D DoA spectrum.

Fig. 3(b) are actually part of the spatial spectrum grating lobes shown in Fig. 3(a), rather than representing the actual DoA of any specific path. Furthermore, comparing Fig. 3(a) with (b), it is clear that the positions of peaks labeled 2 and 3 in Fig. 3(b) do not correspond to any peak positions of the main lobes in Fig. 3(a). This indicates that DoA estimation results based on the equivalent aperture are unreliable in multipath environments.

What's more, while (10) provides accurate results, it presents two main challenges. The spatial spectrum depicted in Fig. 3(a) is obtained by performing angle searches in 181 directions at 1° intervals over a range of -90° to 90° . Additionally, to jointly estimate DoD and DoA, each DoD direction is examined $181 \times$ for every DoA direction, which results in a total of $181 \times 181 = 32761$ angle searches,

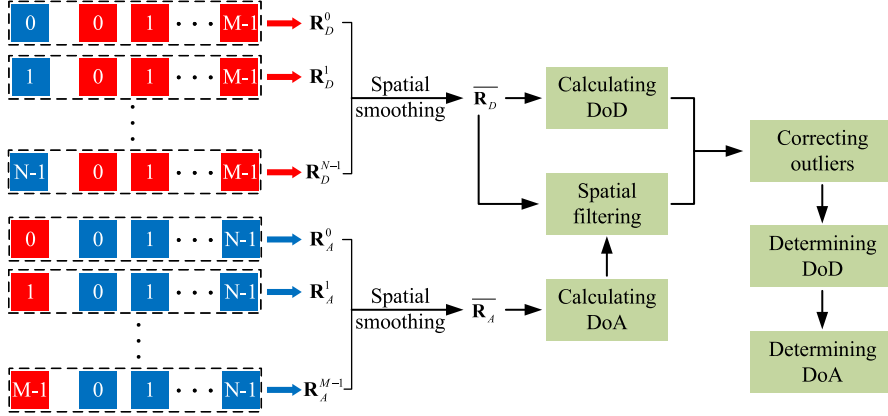


Fig. 4. Signal processing flow of the proposed method.

leading to substantial computational overhead. Furthermore, there are grating lobes in the DoD dimension due to sparse transmitting arrays. However, effective signals only occupy a limited number of angular bins.

Therefore, it is necessary to develop a novel angle estimation method for multipath environments that can reduce unnecessary angle search operations while ensuring accurate angle estimation.

III. PROPOSED METHOD

To address the challenges outlined in Section II, this section introduces a new angle estimation method designed for sparse MIMO arrays in multipath environments. First, this section analyzes the spatial spectral characteristics of DoD and DoA in multipath signals, followed by a detailed presentation of the proposed method.

A. Analysis for the Spatial Spectral Characteristics of DoD and DoA Under Multipath Environments

From (10), it can be seen that the DoD and DoA jointly determine the position of the spectral peak. In order to avoid the mutual interference between DoD and DoA, it is necessary to estimate them separately. The overall signal processing flow is illustrated in Fig. 4.

First, the DoA of the multipath signal is estimated. The data from all receiving channels corresponding to the m th transmitting channel are collected, and its expression is

$$\mathbf{r}_R^m = A_F(\tau) e^{-jm\Delta\phi} [1, e^{-j\Delta\phi}, \dots, e^{-j(N-1)\Delta\phi}]^T. \quad (11)$$

The spatial correlation matrix is calculated by

$$\mathbf{R}_A^m = E \left(\mathbf{r}_R^m(\tau) \cdot (\mathbf{r}_R^m(\tau))^H \right). \quad (12)$$

In order to reduce the correlation between signals from different directions, we apply spatial smoothing technology to process the spatial correlation matrix [24]. This process can be represented as

$$\overline{\mathbf{R}}_A = \frac{1}{M} (\mathbf{R}_A^0 + \mathbf{R}_A^1 + \dots + \mathbf{R}_A^{M-1}). \quad (13)$$

And the receiving steering vector at β is

$$\mathbf{a}_r = [1, e^{j\Delta\phi}, \dots, e^{j(N-1)\Delta\phi}]^T. \quad (14)$$

The Capon algorithm offers the advantages of high resolution and ease of implementation, making it a popular method for angle estimation [25]. Based on this algorithm and the Capon algorithm, the signal power at β is

$$P_A(\beta) = \frac{1}{\mathbf{a}_r^H (\overline{\mathbf{R}}_A)^{-1} \mathbf{a}_r}. \quad (15)$$

Similarly, to eliminate the negative impact of DoA, all the transmitting data corresponding to one of the receiving channels are selected to estimate the DoD, and its expression is

$$\mathbf{r}_T^n = A_F(\tau) e^{-jn\Delta\phi} [1, e^{-j\Delta\phi}, \dots, e^{-j(M-1)\Delta\phi}]^T. \quad (16)$$

Furthermore, the spatial correlation matrix is

$$\mathbf{R}_D^n = E \left(\mathbf{r}_T^n(\tau) \cdot (\mathbf{r}_T^n(\tau))^H \right). \quad (17)$$

Similarly, the spatial correlation matrix after spatial smoothing in the DoD dimension is

$$\overline{\mathbf{R}}_D = \frac{1}{N} (\mathbf{R}_D^0 + \mathbf{R}_D^1 + \dots + \mathbf{R}_D^{N-1}) \quad (18)$$

and the steering vector at α can be obtained by

$$\mathbf{a}_t = [1, e^{j\Delta\phi}, \dots, e^{j(N-1)\Delta\phi}]^T. \quad (19)$$

Similarly, the signal power with the Capon algorithm at α is

$$P_D(\alpha) = \frac{1}{\mathbf{a}_t^H (\overline{\mathbf{R}}_D)^{-1} \mathbf{a}_t}. \quad (20)$$

Performing the above signal processing steps on the same data of Fig. 3, the DoD and DoA estimation results are shown in Fig. 5(a).

Since the array lengths of the receiving array and the transmitting arrays, denoted as L_T and L_R respectively, are $(M-1) \times Nd_r$ and $(N-1) \times d_r$, the resolution of the DoD spectrum is higher than that of the DoA spectrum. When performing DoA estimation on the combined path signal generated by paths P_{10} and P_{01} , the limited spectral resolution of DoA causes its peak position to be located between two true directions, making it impossible to distinguish between them, as shown in Fig. 5(a). Moreover, signals in these two directions can be distinguished on the DoD spectrum, but the true peak position of the spectrum cannot be determined due

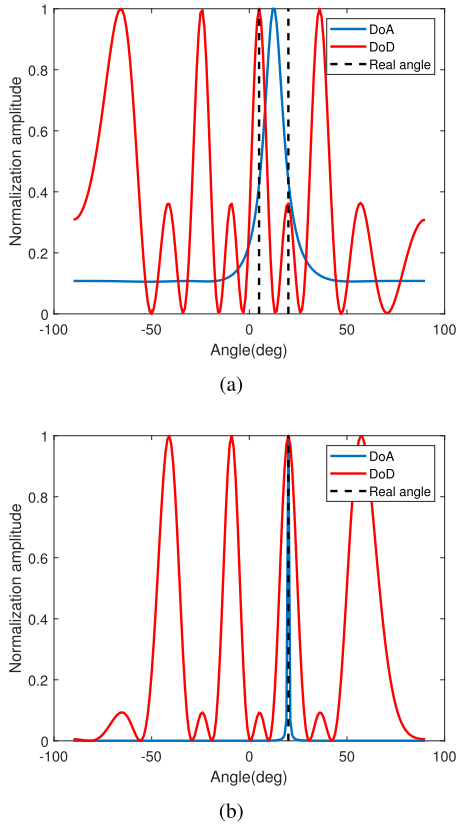


Fig. 5. Angle spectra in a multipath environment based on simulation data. (a) DoD and DoA estimation results of the combined multipath signal and (b) noncombined multipath signals.

to the grating lobe problem caused by the sparse transmitting array arrangement.

To analyze the DoD and DoA characteristics of noncombined paths (\mathcal{P}_{00} or \mathcal{P}_{11}) obtained by the aforementioned method, while keeping other signal parameters unchanged, a signal with both DoD and DoA set to 20° was additionally introduced in the simulation, yielding the results shown in Fig. 5(b). For noncombined paths, the DoD spectrum also suffers from grating lobe issues, while the peak position of the DoA spectrum is close to the true peak position.

Leveraging the respective advantages of these two spatial spectra, this article initially uses the DoA estimation results to design a spatial filter to deal with the grating lobes of the DoD spectrum, and then the accurate DoD and DoA can be obtained through further processes.

B. DoD Estimation Method in Multipath Environments Under DoA Constraints

This section will provide a detailed description of the proposed angle estimation method, which primarily consists of three key steps: grating lobe suppression, DoD estimation, and DoA estimation.

1) *Suppressing the Grating Lobes for DoD Spectrum:* To suppress the grating lobes of the DoD spectrum obtained from (20), a spatial filter must be designed. Let the weight vector of this filter be $\mathbf{w}(\mathbf{w} = [w_0, w_1, \dots, w_M]^T)$, and the direction

of the interest target be θ . The output of the spatial filter is given by

$$\mathbf{y} = \mathbf{w}^H \mathbf{r}_T^n. \quad (21)$$

Therefore, the output power $P(\theta)$ of $\mathbf{y}(\theta)$ can be obtained by

$$\begin{aligned} P(\theta) &= E \{|\mathbf{y}(\theta)|^2\} \\ &= E \left\{ (\mathbf{w}(\theta))^H \mathbf{r}_T^n (\mathbf{r}_T^n)^H \mathbf{w}(\theta) \right\} \\ &= (\mathbf{w}(\theta))^H \mathbf{R}_D^n \mathbf{w}(\theta). \end{aligned} \quad (22)$$

To ensure that the signal from θ passes through the spatial filter without distortion, $\mathbf{w}(\theta)$ should satisfy

$$\mathbf{w}(\theta)^H \mathbf{a}_t(\theta) = 1. \quad (23)$$

In the Capon algorithm [25], the solution for $\mathbf{w}(\theta)$ is expressed as

$$\mathbf{w}(\theta) = \frac{(\mathbf{R}_D^n)^{-1} \mathbf{a}_t(\theta)}{(\mathbf{a}_t(\theta))^H (\mathbf{R}_D^n)^{-1} \mathbf{a}_t(\theta)}. \quad (24)$$

As shown in Fig. 5, the signal energy of the DoA spectrum at the grating lobes of the DoD spectrum is low. Therefore, \mathbf{w} can be weighted using the DoA spectrum estimation results. After weighting, $\mathbf{w}'(\theta)$ is

$$\mathbf{w}'(\theta) = \frac{(\mathbf{R}_D^n)^{-1} \mathbf{a}_t(\theta) P_A(\theta)}{(\mathbf{a}_t(\theta))^H (\mathbf{R}_D^n)^{-1} \mathbf{a}_t(\theta)}. \quad (25)$$

To reduce the correlation between signals from different directions, \mathbf{R}_D^n is replaced by $\overline{\mathbf{R}}_D$ in (22)–(25). Then, $P(\theta)$ is

$$P(\theta) = (\mathbf{w}'(\theta))^H \overline{\mathbf{R}}_D \mathbf{w}'(\theta). \quad (26)$$

Applying this method to suppress grating lobes in the Fig. 5, the results are shown in Fig. 6. We can see that the grating lobes are suppressed successfully.

2) *Determining the Effective Spectral Peak of DoD Spectrum:* After analyzing the measured data, two issues with the DoD spectra arise before and after grating lobe suppression. While keeping other simulation conditions unchanged, the DoD and DoA of path \mathcal{P}_{01} are set to 39° and 43° , respectively, while for path \mathcal{P}_{01} , they are set to 43° and 39° , respectively. And the simulation results are illustrated in Fig. 7.

The first issue is spectral peak drift. Due to varying SNRs between different multipath signals, there is a significant difference in signal strength across the DoD-DoA heat map, as shown in Fig. 7. The signal with higher signal strength exhibits smaller DoD and larger DoA, leading to discrepancies in the spectral peak positions of the DoD and DoA spectra. Since (25) is derived from the DoA estimation, the peak positions of the filtered results differ from those of the DoD spectrum.

Another issue is the distortion of the DoD spectrum. As shown in Fig. 7, the small angular difference between combined paths, along with the significantly lower energy of one path compared to the other, results in a single spectral peak on the DoD spectrum. Additionally, because the DoA with stronger energy is larger than that with weaker energy, weak path energy is amplified during the filtering process. This results in spectral peaks appearing in directions where the original DoD spectrum did not have peaks.

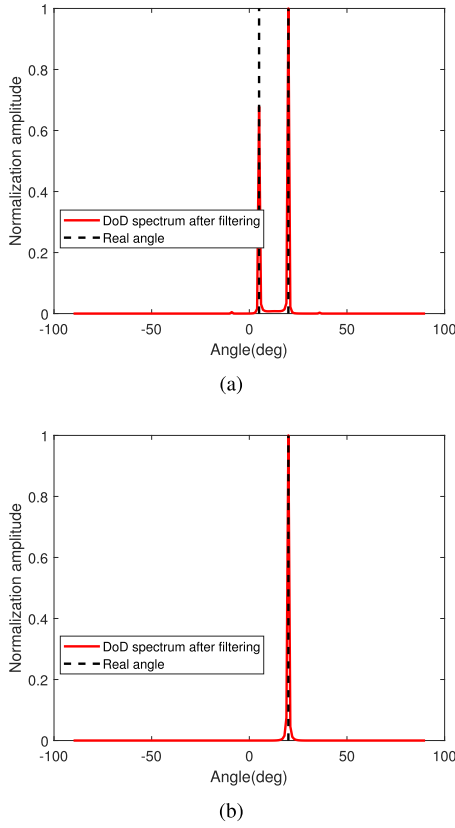


Fig. 6. DoD spectra after spatial filtering. (a) and (b) Correspond to Fig. 5(a) and (b), respectively.

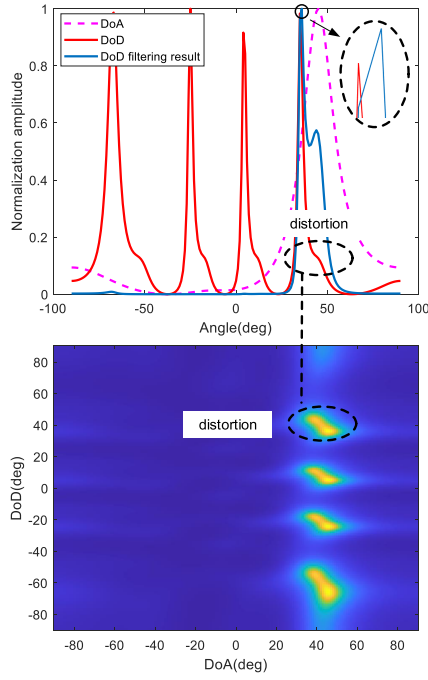


Fig. 7. Results of peak drift and distortion in the filtered DoD spectrum.

To address these two issues, we propose the following solutions. Since the aperture of the transmitting antenna is larger than that of the receiving antenna, the DoD spectrum estimation achieves higher accuracy compared to the DoA spectrum estimation. Therefore, after filtering, the DoD

spectral peaks closest to the filtering result are selected as the effective DoD estimation.

For the other issue, after a careful analysis of the distortion, it was found that in an ideal state, the first derivative of the DoD spectrum is monotonic, and the monotonicity at the point of distortion will change. Therefore, if spectral peaks appear in the filtered spectrum within the angle range where the monotonicity of the first derivative of the DoD spectrum changes, the angle corresponding to this change in monotonicity is considered as an effective DoD estimation.

After the above two operations, effective DoD estimation results $\mathbf{I}_D = [\theta_1, \theta_2, \dots, \theta_L]$ will be obtained, where L represents the number of estimated DoDs.

3) *Estimating the DoAs of Signals:* Due to the DoD and DoA of the combined path being different in multipath environments, it is impossible to know the DoA based on the DoD estimation result alone, making it necessary to estimate the DoA of the signal.

The spatial correlation matrix obtained from all transmitting and receiving channels is expressed as

$$\mathbf{R}_c = E(\mathbf{R}\mathbf{R}^H). \quad (27)$$

Herein, \mathbf{R} is

$$\mathbf{R} = [R_{00}(\tau) R_{01}(\tau) \dots R_{M-1N-1}(\tau)]^T. \quad (28)$$

Let the transmitting and receiving steering vectors for the p th and the q th directions be $\mathbf{a}_t(\theta_p)$ and $\mathbf{a}_r(\theta_q)$ ($p, q \leq L$), respectively. The joint steering vector can be obtained as

$$\mathbf{a}_{tr}(\theta_p, \theta_q) = \mathbf{a}_t(\theta_p) \otimes \mathbf{a}_r(\theta_q). \quad (29)$$

Therefore, the power of DoD-DoA heat map at (θ_p, θ_q) is

$$P_{DA}(\theta_p, \theta_q) = \frac{1}{\mathbf{a}_{tr}^H(\theta_p, \theta_q) \mathbf{R}_c^{-1} \mathbf{a}_{tr}(\theta_p, \theta_q)}. \quad (30)$$

Since each propagation path exhibits a unique correspondence between DoD and DoA, P_{DA} attains its global maximum precisely only when θ_p and θ_q match the actual DoD and DoA. Therefore, by exhaustively evaluating all (θ_p, θ_q) pairs, the DoD and DoA can be determined by identifying the combination that maximizes P_{DA} .

IV. SIMULATIONS AND EXPERIMENTAL RESULTS

In this section, the correctness and effectiveness of the proposed method will be verified through Monte Carlo simulations and measured data. First, to analyze the algorithm of different methods, 2000 Monte Carlo simulation experiments were conducted. Additionally, experiments with various target positions, target numbers, and experimental scenarios were conducted to verify the effectiveness of the algorithm in real-world testing scenarios.

A. Algorithm Performance Analysis Through Simulations

First, this section introduces several commonly used signal angle estimation methods in multipath scenarios, provides a detailed comparison of the computational accuracy and complexity of each method, and then demonstrates through simulation experiments that the proposed method offers superior overall performance in both computational accuracy and complexity compared to existing approaches.

TABLE II
NUMBER OF ANGULAR SEARCHES REQUIRED BY DIFFERENT METHODS

	Method in [16]	Method in [18]	Method in [20]	Our method
Number of angle searches	$181 \times 181 = 32,641$	$91 \times 181 = 16,471$	$181 \times M + 181$	$181 \times 2 + L^2 (L^2 < 181)$
Aperture size for DoD estimation	$(M - 1) \times d_t$	$(M - 1) \times d_t$	$(M - 1) \times d_t$	$(M - 1) \times d_t$
Aperture size for DoA estimation	$(N - 1) \times d_r$	$(N - 1) \times d_r$	$(N - 1) \times d_r$	$(M - 1) \times d_t$

1) *Method in [16]*: The first method is based on the 2-D DoD-DoA angular spectrum. First, a 2-D DoD-DoA spectrum is created by comprehensively searching all possible DoD and DoA combinations, then DoD and DoA of the signal are estimated from this spectrum. Consequently, the estimation accuracy of DoD and DoA depends on the lengths of the transmit and receive arrays, respectively.

Assuming the search ranges for both DoD and DoA are $[-90^\circ, -90^\circ]$ with a step size of 1° , the number of angle searches required to generate a 2-D DoD-DoA spectrum is $181 \times 181 = 32,641$.

2) *Method in [18]*: The second method is the ESTAR algorithm proposed by Takahashi et al. [18]. This method follows the same principle for generating the DoD-DoA 2-D angular spectrum as the method in [16] but only computes half of the spectrum. Thus, while the estimation accuracy of DoD and DoA remains the same as the method in [16], the number of angle searches is halved.

3) *Method in [20]*: The third method is proposed by Park et al. [20]. This approach first estimates M 1-D DoA spectra using the receive antennas corresponding to each transmit antenna, then performs incoherent accumulation on these M 1-D DoA spectra. Based on this accumulated result, the DoA of the signal is obtained. Subsequently, using the estimated DoA, it estimates a 1-D DoD spectrum to determine the DoD of the signal. Since this algorithm estimates DoA first and the receive array aperture is limited (resulting in relatively low angular resolution), the estimated DoA becomes biased when the DoAs of two signals are close. Moreover, because the estimated DoD strongly depends on the DoA estimation result, even if the transmit array aperture is sufficient to resolve signals from two directions, the biased DoA estimate leads to a biased DoD estimate. What's more, the number of angle searches for this method is $181 \times M + 181$.

4) *Our Method*: The last method is the method proposed in this article. First, the method uses the receive array to determine the signal direction interval, then designs a spatial filter based on this interval to obtain a DoD angular spectrum free of grating lobes. By comparing the DoD angular spectra before and after filtering, the DoD of the signal is determined. Finally, leveraging the mathematical relationship between the DoD and DoA of multipath signals, a lookup table is constructed to identify the optimal DoD-DoA combination as the final estimation result. As shown in Table II, since the angular resolution of our method primarily depends on the transmit array aperture, its DoA estimation accuracy surpasses that of the aforementioned three methods. Additionally, this method performs angle searches only during the computation

of the DoA spectrum (181 searches), the DoD spectrum (181 searches), and the final selection of the optimal DoD-DoA combination (L^2 searches), resulting in a total of $181 \times 2 + L^2$ angle searches. L represents the number of targets within the same range bin. As the proposed angle estimation is performed after the Range-FFT, each range bin contains signals from a limited number of directions, so that $L^2 < 181$.

For ease of comparison, the number of angle searches required by these four methods are summarized in Table II. Notably, when the number of transmitting antennas is three or more, the proposed algorithm requires significantly fewer angle searches. In practice, MIMO radar systems often employ more than three transmitting antennas to achieve large array apertures.

Furthermore, this article compares the specific performance of these four methods in angle estimation accuracy through simulation experiments. There are two signals in the simulation. One signal is generated along path \mathcal{P}_{10} and another along path \mathcal{P}_{01} . For \mathcal{P}_{10} , the DoD $\alpha_1 = 5^\circ$, and the DoA $\beta_1 = 20^\circ$; for path \mathcal{P}_{01} , the DoD $\alpha_2 = 20^\circ$, and the DoA $\beta_2 = 5^\circ$. The other simulation parameters are the same as Table I.

Through 2000 Monte Carlo experiments, the results shown in Table III are obtained. The results in Table III lead to the following conclusions.

- 1) Since $L_T > L_R$, the resolution of the DoD spectrum is higher than that of the DoA spectrum. Consequently, the method in [16] yields smaller RMSE values for the DoD estimates of both signals compared to their DoA estimates.
- 2) As the method in [18] only estimates half of the DoD-DoA spectrum, it fails to capture the spectral peaks located in the other half of the spectrum. This results in estimation outcomes that include only one target's DoD and DoA. In other words, this method becomes ineffective when dealing with composite paths formed by \mathcal{P}_{01} and \mathcal{P}_{10} .
- 3) Since the resolution of the DoA spectrum is insufficient to distinguish signals from these two directions, it not only leads to significant deviations in the DoA estimation results but also causes target missed detection and affects the accuracy of the DoD. Consequently, the performance of the method in [20] deteriorates markedly when the DoA spectrum fails to resolve signals from two distinct directions.
- 4) By fully leveraging the high-resolution characteristics of the DoD spectrum, our proposed method achieves superior estimation accuracy for both the DoD and DoA spectra compared to the above three methods.

TABLE III

DoD AND DOA ESTIMATION RESULTS COMPARED WITH DIFFERENT METHODS BASED ON MONTE CARLO EXPERIMENTS

	\mathcal{P}_{10}		\mathcal{P}_{01}	
	DoD (deg)	DoA (deg)	DoD (deg)	DoA (deg)
Method in [16]	0	2.0025	0	2
Method in [18]	0	2	-	-
Method in [20]	0.6535	7.129	-	-
Ours	0	0	0	0

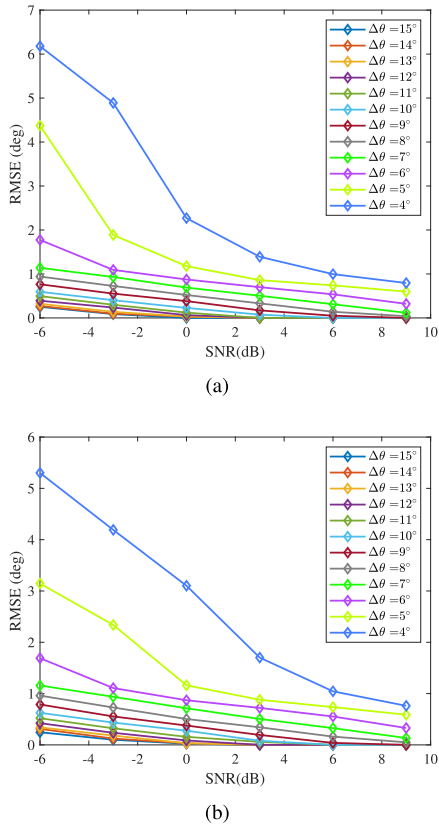


Fig. 8. Simulation experimental results under different angle differences and SNRs. (a) RMSE of the DoD estimation results and (b) RMSE of the DoA estimation results.

In addition, to investigate the performance of the proposed method under varying SNRs and angular separations between the two signals, we conducted the following simulations. In these simulations, the β_1 of path \mathcal{P}_{10} and the α_2 of path \mathcal{P}_{01} are still equal to 20° . Simultaneously, the α_1 of path \mathcal{P}_{10} and the β_2 of path \mathcal{P}_{01} are both initially set at 5° and then gradually increased to 14° in increments of 1° . Moreover, for each change in angle, the SNR is initially set at -6 dB and then increased to 9 dB in increments of 3 dB. All other simulation conditions remain the same as those described previously, and the simulation results are displayed in Fig. 8.

Due to $\beta_1 = \alpha_2$ and $\alpha_1 = \beta_2$, only the RMSE of the DoD and DoA of \mathcal{P}_{10} is presented in Fig. 8. In addition, in Fig. 8, $\Delta\theta = \beta_1 - \alpha_1$. It can be observed from Fig. 8 that for signals with a fixed $\Delta\theta$, the RMSE of the estimation results decreases as the SNR increases. For the same SNR condition,

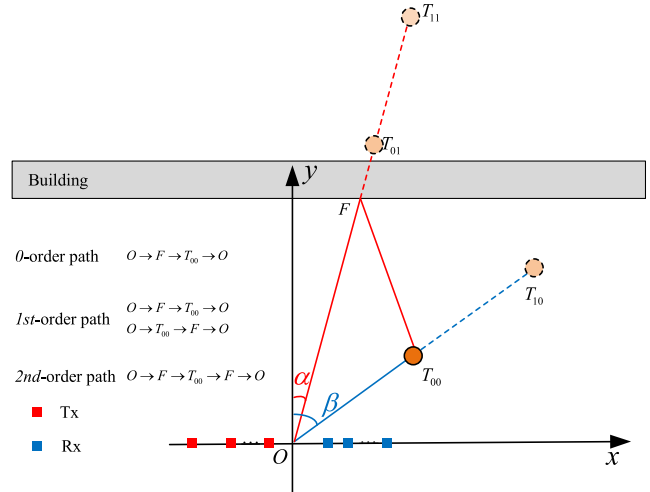


Fig. 9. Propagation model for the target closed to the radar.

the RMSE of the estimation results increases as the value of $\Delta\theta$ decreases. Furthermore, the simulation results indicate that when $\Delta\theta \geq 7^\circ$ and the echo SNR exceeds -6 dB, the RMSEs of DoD and DoA estimation results are approximately 1° , yielding comparatively accurate and stable estimation results. Conversely, when $\Delta\theta \leq 6^\circ$, a higher SNR is required to achieve comparable accuracy, and the smaller $\Delta\theta$, the more stringent the SNR requirement becomes.

The aforementioned simulation results demonstrate that the proposed algorithm can achieve effective estimation of target angles in multipath environments across various simulation scenarios.

B. Algorithm Feasibility Verification Through Experiments

This section validates the proposed algorithm's effectiveness using diverse experimental measurements. The experiments consist of three parts.

- 1) Single-target tests at varying target positions, assessing the performance of the proposed method in single-target scenarios.
- 2) Dual and triple target experiments, primarily evaluating algorithm robustness when radar range resolution is insufficient to distinguish targets and under varying propagation path conditions.
- 3) Outdoor scenario measurements, verifying the performance of the proposed method in real-world outdoor environments.

1) Single-Target Tests at Varying Target Positions:

This article is based on our previous research work [19], and the specific images of the radar and experimental setup are presented in [19, Fig. 5]. The radar is the TI MMWCAS-RF-EVM [26], and the signal parameters are the same as those in [19, Table I]. Furthermore, the half-power beamwidth of the antennas is 4.6° . The detail radiation patterns of the transmitting and receiving antennas are detailed in [27].

As shown in Fig. 9, compared to the target position in Fig. 1, the value of $\beta - \alpha$ between first-order paths increases when the target is closer to the radar. Taking into account the influence

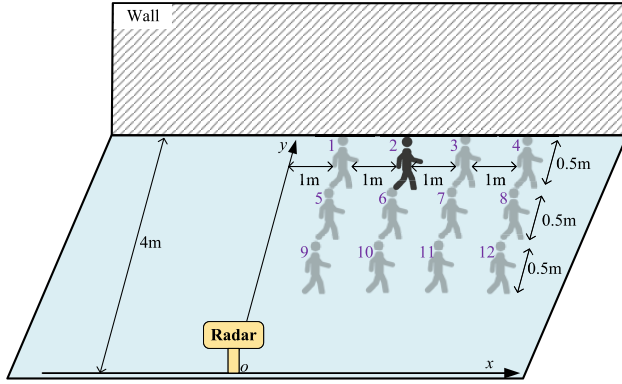


Fig. 10. Schematic of target position distributions in single-target experiments.

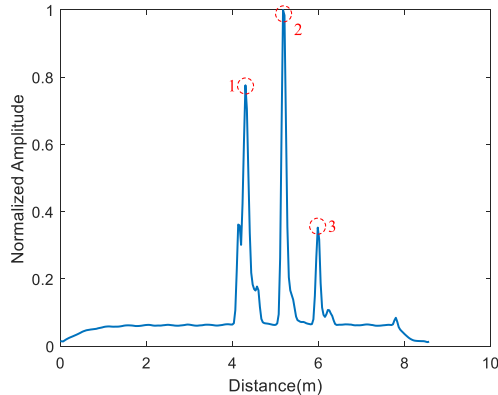


Fig. 11. Range profile at the ninth frame corresponds to the position of (2, 3.5) m.

TABLE IV
REFERENCE VALUES OF SIGNAL PARAMETERS FOR
DIFFERENT PROPAGATION PATHS

	\mathcal{P}_{00}	\mathcal{P}_{10}	\mathcal{P}_{01}	\mathcal{P}_{11}
Distance (m)	4.24	5.04	5.04	5.83
DoD (deg)	45	30.96	45	30.96
DoA (deg)	45	45	30.96	30.96

of multipath reflections on the relative positions of targets, walls, and the radar, data from 12 different target positions, which are shown in Fig. 10, were collected to validate the effectiveness of the proposed algorithm. It is worth mentioning that, since the reflection signal from the torso is stronger than that from the limbs [28], [29], the radar's main beam was ensured to be directed at the target's thoracic region during the experiment.

Using the data at coordinates (2, 3.5) m in Fig. 10 as an example, we first employ the data processing procedure used in [19] to suppress the static clutter generated by fixed objects such as the ground and walls. Then, after Range-FFT and noncoherent accumulation, the range profile shown in Fig. 11 is obtained. It can be seen that the echo signal primarily contains three signal components. To analyze the propagation paths corresponding to these signals, the propagation distances, DoDs, and DoAs were calculated based on the EM propagation model shown in Fig. 1, with the results listed in Table IV.

The distances corresponding to the three peaks shown in Fig. 11 are 4.30, 5.18, and 5.98 m, respectively. Considering the measurement errors due to the scalability of the human target, peaks 1 and 3 in Fig. 11 correspond to signals propagating along the paths \mathcal{P}_{00} and \mathcal{P}_{11} , while peak 2 corresponds to propagation paths \mathcal{P}_{10} and \mathcal{P}_{01} .

The DoD-DoA spatial spectra corresponding to these three peaks and the 1-D angle spectrum based on the virtual array were computed separately, yielding the results shown in Fig. 12(a), which presents the 2-D DoD-DoA spectrum for the direct path \mathcal{P}_{00} . The main lobe of this spectrum is expected to align with the white dashed line in Fig. 12(a). The blue curve in Fig. 12(d) represents the 1-D DoA spectrum of the receiving signal, estimated using the equivalent array method. What's more, the red circular markers denote the spectrum derived from the data along the white dashed line in Fig. 5(a). Since the DoD and DoA are identical for the direct path, these two spectra (blue and red) exhibit perfect overlap.

Fig. 12(b) shows the 2-D DoD-DoA spatial spectrum corresponding to combined paths \mathcal{P}_{10} and \mathcal{P}_{01} . Since paths \mathcal{P}_{10} and \mathcal{P}_{01} have identical DoD and DoA, the main lobe of this spectrum exhibits symmetric distribution about the white dashed line. Similarly, the blue spectrum in Fig. 12(e) represents the 1-D DoA spectrum obtained using the equivalent array method, while the red circles show the spectrum plotted from the data along the white dashed line in Fig. 12(b). As the echo signal corresponding to peak 2 in Fig. 11 is formed by paths \mathcal{P}_{10} and \mathcal{P}_{01} with unequal DoA values, the blue spectrum in Fig. 12(e) theoretically exhibits two spectral peaks. However, the equivalent array DoA estimation method only considers the signal DoA while neglecting the DoD, resulting in model mismatch in multipath environments and thus incorrect spectral estimation results. Notably, the blue spectrum and red circles in Fig. 12(e) show perfect overlap, demonstrating that the angle spectrum estimation based on (5) represents a special case of the formulation (10).

Fig. 12(c) and (f) present the 2-D DoD-DoA spatial spectrum and 1-D DoA spectrum, respectively, corresponding to path \mathcal{P}_{11} . Since path \mathcal{P}_{11} shares identical physical characteristics in DoD and DoA with path \mathcal{P}_{00} , the DoA estimation derived from (5) matches the estimation obtained from (10), both accurately reflecting the true DoA of the target. The analysis of these experimental results demonstrates that the findings discussed in the Section III-A hold validity not only in simulated environments but also in real-world scenarios.

To validate the effectiveness of the proposed angle estimation method across different target positions, the developed algorithm was applied to process data from the 12 distinct locations shown in Fig. 10. It is worth noting that we measured the positions of the target and the wall using a tape measure, and derived the positions of multipath ghost targets corresponding to different propagation paths based on ray-tracing theory. Based on this, the true DoA values of both the target and the multipath ghost targets were obtained, which were then used to calculate the root mean square error (RMSE) of the DoA estimation results. As shown in Fig. 13, the maximum RMSE of the DoA estimation results for different positions

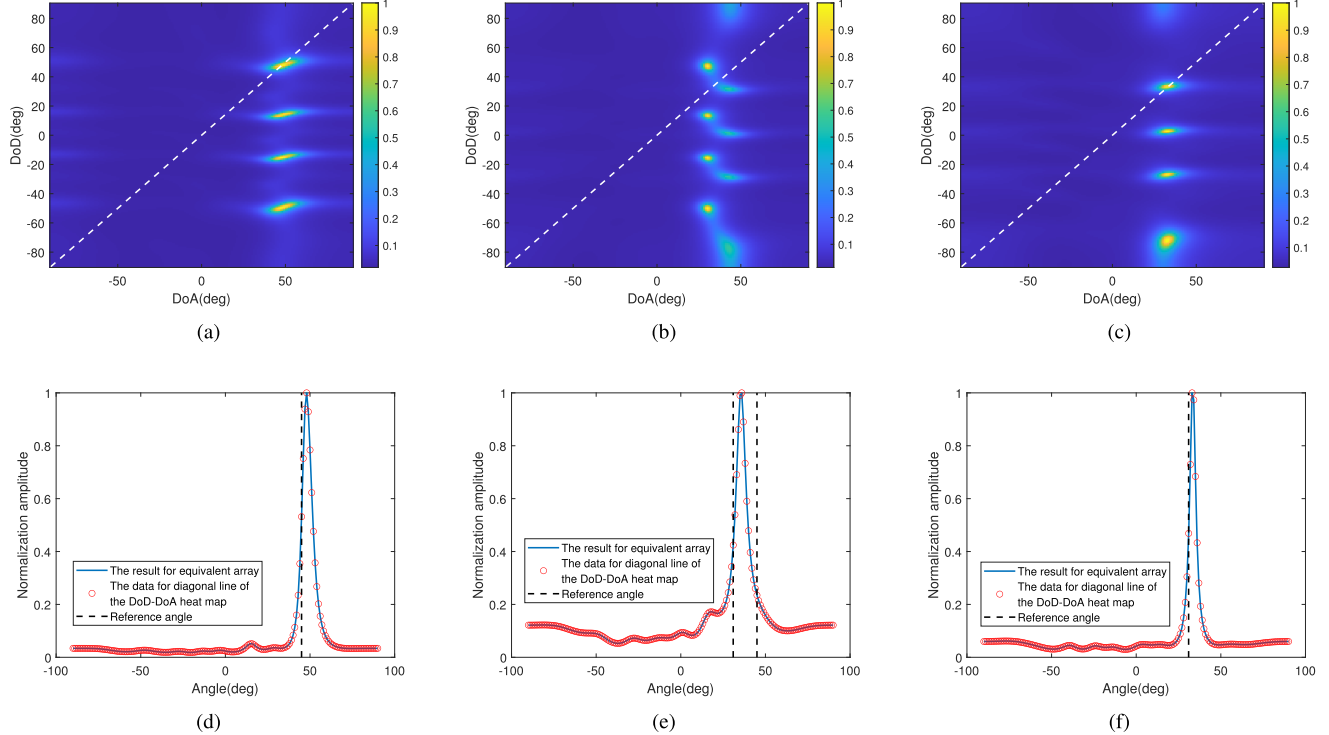


Fig. 12. 2-D DoD-DoA angular spectra for different propagation paths and their corresponding 1-D angular spectra based on the equivalent virtual array. (a)–(c) 2-D DoD-DoA angular spectra for path \mathcal{P}_{00} , paths \mathcal{P}_{01} and \mathcal{P}_{10} , and path \mathcal{P}_{11} , respectively. (d)–(f) 1-D angular spectra derived from the equivalent virtual array for path \mathcal{P}_{00} , paths \mathcal{P}_{01} and \mathcal{P}_{10} , and path \mathcal{P}_{11} , respectively.

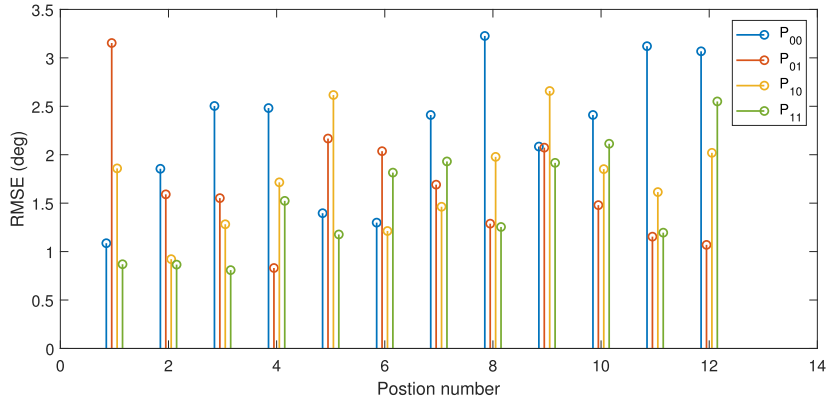


Fig. 13. DoA estimation RMSEs for different target positions shown in Fig. 10 based on the proposed method.

and propagation paths using the proposed algorithm does not exceed 3.5° . Considering that the human target involved in the experimental data collection has a width and is in a micro-motion state during data acquisition, this error level falls within acceptable limits.

2) *Dual and Triple Target Experiments*: To validate the effectiveness of the proposed method in multitarget scenarios, experiments with varying target quantities were designed in the same environment as the single-target experiments. Following Range-FFT processing, signals from different propagation paths exhibited significant range separation, ensuring each range bin contained signals from a limited number of targets. In single-target scenarios, except for the two propagation paths \mathcal{P}_{10} and \mathcal{P}_{01} that shared identical propagation distances and thus occupied the same range bin, the range bins

corresponding to \mathcal{P}_{00} and \mathcal{P}_{11} contained signals from only a single propagation path. The primary distinction between multitarget and single-target scenarios lies in the possibility of multiple paths or targets occupying the same range bin. Consequently, the experiments in multitarget scenarios primarily focused on conditions where radar range resolution was insufficient to distinguish between different targets or propagation paths.

For this part, data were collected for both dual-target and triple-target scenarios. In the dual-target experiment, two targets were located at a distance of 3.5 m from the radar, with azimuth angles of 30° and -45° relative to the radar, respectively, which can be shown in Fig. 14(a). The processed results using the proposed algorithm are presented in Fig. 14(b) and (c).

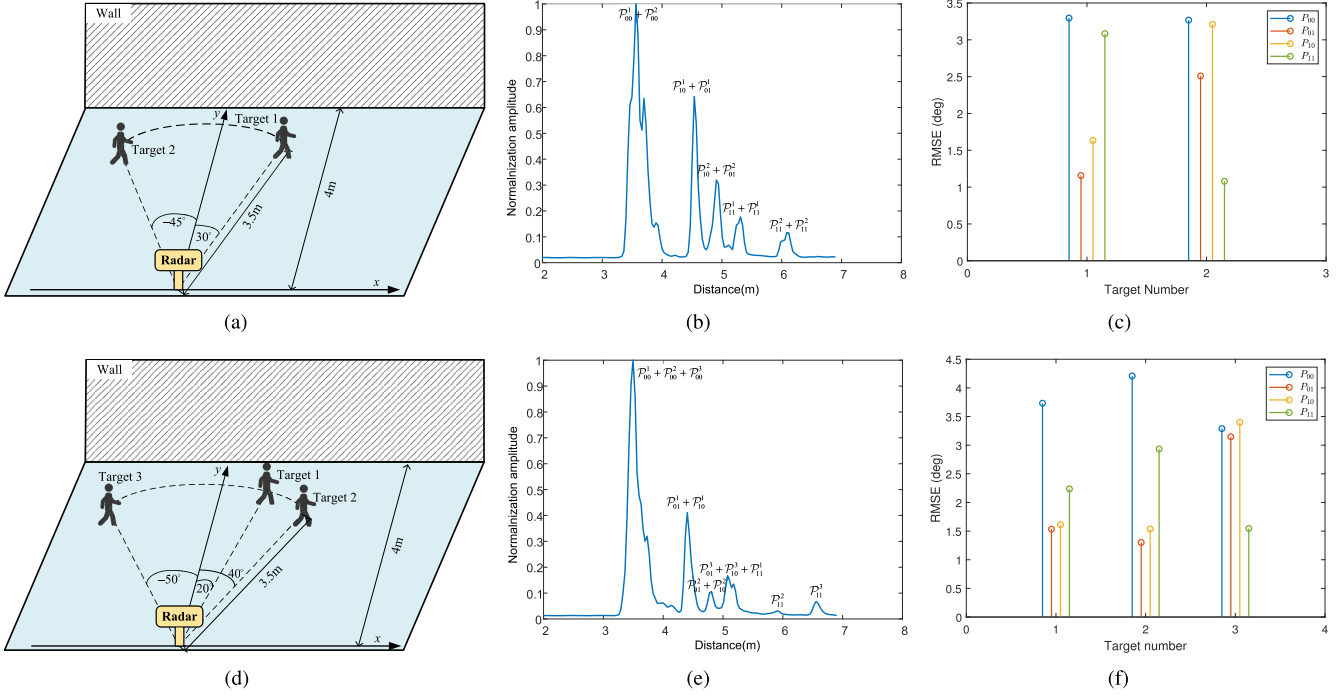


Fig. 14. Results of different target numbers. (a)–(c) Target position distributions, 1-D range profile, and RMSEs of angle estimation results from different propagation paths for the dual-target experiment, respectively. (d)–(f) Corresponding elements for the triple-target experiment.

In Fig. 14(b), the symbols adjacent to each range spectral peak represent the corresponding signal components, where the superscript denotes the target identifier, and the first and second digits of the subscript indicate the transmitting and receiving path numbers, respectively. In this experiment, since both targets were at the same distance from the radar and the signal of \mathcal{P}_{00} experienced the least energy attenuation, the spectral peak with the highest amplitude corresponded to the composite signal of path \mathcal{P}_{00} from both targets. Additionally, as target 1 was closer to the wall than target 2, the propagation range of \mathcal{P}_{00}^1 was shorter than that of \mathcal{P}_{00}^2 , resulting in higher signal amplitudes for the paths \mathcal{P}_{10}^1 , \mathcal{P}_{01}^1 and \mathcal{P}_{11}^1 compared to those of target 2.

The RMSE of the target angle estimation result is shown in Fig. 14(c). A comparison with the single-target results in Fig. 13 reveals that the RMSE values of the dual-target data are comparable to those of the single-target case. This indicates that the proposed method is feasible in the dual-target scenario.

To analyze the algorithm's performance with a larger number of targets, the data of the three-target scenario was collected. As shown in Fig. 14(d), the three targets were located at azimuth angles of 20°, 40°, and -50° relative to the radar, all at a distance of 3.5 m. After applying the proposed algorithm, the results are presented in Fig. 14(e) and (f).

Similarly, Fig. 14(e) annotates the signal components corresponding to each range spectral peak. Notably, due to the propagation distances proximity between the paths \mathcal{P}_{10}^3 , \mathcal{P}_{01}^3 and \mathcal{P}_{11}^1 , these three paths shared the same range bin in the range profile. The RMSE of the target angle estimation result is shown in Fig. 14(f).

Compared to the single-target and dual-target cases, the maximum RMSE increased by approximately 1° for the

triple-target scenario. Detailed analysis of each frame revealed that the sparse arrangement of the transmit array introduced grating lobes in the DoD spectrum. As the number of targets increased, these grating lobes occupied a significant portion of the angular spectrum. Furthermore, when the number of grating lobes grew, some lobes from one target approached the main lobe of another target, causing the main lobe direction to deviate from its theoretical value and thereby degrading the algorithm's estimation performance.

3) *Outdoor Scenario Measurements:* To analyze the performance of the proposed algorithm in different scenarios, this section collected data with varying target positions and quantities in a common outdoor parking lot, using the same signal parameters as those in Section IV-B. The data acquisition scenario is illustrated in Fig. 15(a), where the car is set as the reflective surface, analogous to the wall in Fig. 10. Fig. 15(b) presents a schematic of single-target experimental scenario from a top-down perspective. In this experiment, the projection point of the radar on the ground is defined as the origin of the coordinate system, which can be shown in Fig. 15(b). The side of the vehicle is parallel to the positive direction of the y-axis, and the distance between the vehicle and the y-axis is 2.6 m. To ensure effective detection performance, the radar antenna is oriented at an angle of 48° with respect to the positive direction of the x-axis.

As shown in Fig. 15(b), it presents the single-target data collection scenario at different positions, and the target positions are marked as yellow dots. During the experiment, a person acting as the target stood in these three positions in sequence. As shown in Fig. 15(d), two people were positioned as targets for the dual-target experimental data collection, differing only in the number and positions of targets compared to the

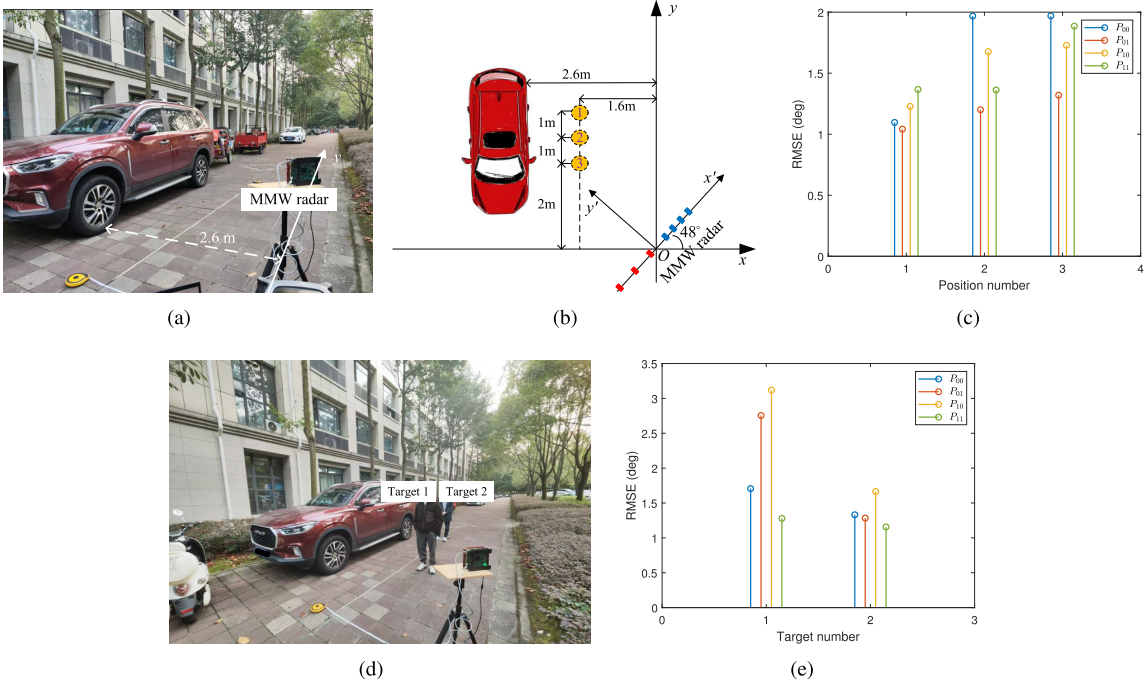


Fig. 15. Results of outdoor scenario. (a) Experimental scene photograph. (b) Schematic of single-target experimental scenario from a top-down perspective, and the three different positions of the single-target experiment are marked as yellow dots. (c) RMSEs of angle estimation results for the single-target scenario. (d) and (e) Corresponding elements for the dual-target scenario.

TABLE V
AVERAGE ANGULAR SEARCH TIME REQUIRED BY DIFFERENT METHODS

	Method in [16]	Method in [18]	Method in [20]	Our method
Time (ms)	75.5440	35.3998	1.3615	0.7533

single-target scenario. The coordinates of the two targets are $(-1.1, 2)$ m and $(-1.6, 4.5)$ m, respectively.

The data from these two scenarios were processed using the proposed algorithm, and the statistical results are shown in Fig. 15(c) and (e) respectively. As can be seen from Fig. 15(c) and (e), compared with the results in Sections IV-B1 and IV-B2, since the vehicle shell is made of metal and reflects EM waves more strongly than the wall, the overall RMSE of the estimation results is smaller. These two sets of results indicate that the proposed method is also applicable in outdoor scenarios.

4) *Analysis of Calculation Efficiency*: Furthermore, the computational efficiency of the proposed algorithm is analyzed. The above experimental data are processed using MATLAB 2020a on a Windows 11 operating system with a 13th Gen Intel¹ Core² i5-13500 CPU operating at 2.50 GHz. The four different angle estimation methods described earlier are applied to process the aforementioned measured data, conducting a total of 473 angle estimations. The average computation time for each algorithm is presented in Table V. It can be seen that, compared to the other algorithms, the proposed algorithm demonstrates higher computational efficiency.

V. CONCLUSION

This article proposed an effective method to address the problem of joint estimation of DoD and DoA in sparse MIMO radar systems in multipath environments. First, the necessity of jointly estimating the DoD and DoA of signals in multipath environments was demonstrated based on the fundamental principles of angle estimation with MIMO arrays. Subsequently, the method proposed in this article was introduced in detail. This method first estimated the DoA of the signals. Then, based on the DoA estimation result, a spatial filter was designed to suppress the grating lobes caused by sparse transmitting arrays. This method could not only accurately obtain the DoD and DoA of the signals but also significantly reduce the number of angle search iterations. Finally, the correctness and effectiveness of the proposed algorithm have been demonstrated through simulations and experimental data. The simulation results demonstrated that, compared to existing methods that could not simultaneously guarantee the estimation accuracy of both DoD and DoA, the proposed method in this article could achieve concurrent assurance of DoD and DoA estimation accuracy. Moreover, when the $\Delta\theta \geq 7^\circ$ and the echo SNR exceeded -6 dB, the RMSEs of the DoD and DoA estimation results from the proposed method were approximately 1° . What's more, the experimental results indicated that the proposed method reduced the runtime of the state-of-the-art angle

¹Registered trademark.

²Trademarked.

estimation algorithm in multipath environments from 1.3615 to 0.7533 ms, achieving a 44.67% improvement in operational efficiency.

Although both simulation and experimental results have verified the feasibility of the proposed method, there are still some issues that need to be addressed. As demonstrated by the simulation results of this study, when the resolution and SNR of the transmitting antenna are insufficient to distinguish signals from two directions, the algorithm proposed in this article cannot obtain accurate estimation results. Therefore, in future research, we will focus on angle estimation of target signals in low SNR and small $\Delta\theta$ to obtain more robust estimation results.

REFERENCES

- [1] S. M. Patole, M. Torlak, D. Wang, and M. Ali, "Automotive radars: A review of signal processing techniques," *IEEE Signal Process. Mag.*, vol. 34, no. 2, pp. 22–35, Mar. 2017.
- [2] M. Manzoni, S. Tebaldini, A. V. Monti-Guarnieri, and C. M. Prati, "Multipath in automotive MIMO SAR imaging," *IEEE Trans. Geosci. Remote Sens.*, vol. 61, 2023, Art. no. 5202612.
- [3] M. Chamseddine, J. Rambach, D. Stricker, and O. Wasenmüller, "Ghost target detection in 3D radar data using point cloud based deep neural network," in *Proc. 25th Int. Conf. Pattern Recognit. (ICPR)*, Jan. 2021, pp. 10398–10403.
- [4] L. Zheng, J. Long, M. Lops, F. Liu, X. Hu, and C. Zhao, "Detection of ghost targets for automotive radar in the presence of multipath," *IEEE Trans. Signal Process.*, vol. 72, pp. 2204–2220, 2024.
- [5] T. Visentin, J. Hasch, and T. Zwick, "Analysis of multipath and DOA detection using a fully polarimetric automotive radar," *Int. J. Microw. Wireless Technol.*, vol. 10, nos. 5–6, pp. 570–577, Jun. 2018.
- [6] N. Scheiner et al., "Seeing around street corners: Non-line-of-sight detection and tracking in-the-wild using Doppler radar," in *Proc. IEEE/CVF Conf. Comput. Vis. Pattern Recognit. (CVPR)*, Jun. 2020, pp. 2065–2074.
- [7] J. Chen, S. Guo, H. Luo, N. Li, and G. Cui, "Non-line-of-sight multi-target localization algorithm for driver-assistance radar system," *IEEE Trans. Veh. Technol.*, vol. 72, no. 4, pp. 5332–5337, Apr. 2023.
- [8] L. Wang, S. Giebenhain, C. Anklam, and B. Goldluecke, "Radar ghost target detection via multimodal transformers," *IEEE Robot. Autom. Lett.*, vol. 6, no. 4, pp. 7758–7765, Oct. 2021.
- [9] Y. Jin, R. Prophet, A. Deligiannis, I. Weber, J.-C. Fuentes-Michel, and M. Vossiek, "Comparison of different approaches for identification of radar ghost detections in automotive scenarios," in *Proc. IEEE Radar Conf.*, May 2021, pp. 1–6.
- [10] F. Kraus, N. Scheiner, W. Ritter, and K. Dietmayer, "Using machine learning to detect ghost images in automotive radar," in *Proc. IEEE 23rd Int. Conf. Intell. Transp. Syst. (ITSC)*, Sep. 2020, pp. 1–7.
- [11] R. Prophet, J. Martínez, J.-C. F. Michel, R. Ebelt, I. Weber, and M. Vossiek, "Instantaneous ghost detection identification in automotive scenarios," in *Proc. IEEE Radar Conf. (RadarConf)*, Apr. 2019, pp. 1–6.
- [12] F. Kraus, N. Scheiner, W. Ritter, and K. Dietmayer, "The radar ghost dataset—An evaluation of ghost objects in automotive radar data," in *Proc. IEEE/RSJ Int. Conf. Intell. Robots Syst. (IROS)*, Prague, Czech Republic: IEEE, Sep. 2021, pp. 8570–8577.
- [13] R. Feng, E. D. Grefe, M. Rykunov, H. Sahli, S. Pollin, and A. Bourdoux, "Multipath ghost recognition for indoor MIMO radar," *IEEE Trans. Geosci. Remote Sens.*, vol. 60, 2022, Art. no. 5104610.
- [14] R. Takahashi, N. Suzuki, and H. Tasaki, "Window function for MIMO radar beamforming to mitigate multipath clutter," in *Proc. Int. Conf. Radar (RADAR)*, Aug. 2018, pp. 1–6.
- [15] Z. Chuanhao, H. Xu, L. Jiamin, L. Mingxuan, H. Xueyao, and Z. Liping, "A multipath signals recognition method based on deep neural network," in *Proc. IEEE Int. Conf. Signal, Inf. Data Process. (ICSIDP)*, Nov. 2024, pp. 1–6.
- [16] Y. Li and X. Shang, "Multipath ghost target identification for automotive MIMO radar," in *Proc. IEEE 96th Veh. Technol. Conf. (VTC-Fall)*, Sep. 2022, pp. 1–5.
- [17] Z. Zhu et al., "Non-line-of-sight targets localization algorithm via joint estimation of DoD and DoA," *IEEE Trans. Instrum. Meas.*, vol. 72, pp. 1–11, 2023.
- [18] R. Takahashi, P. Wang, and K. Suwa, "ESTAR multipath angle estimation for sparse array MIMO radar," in *Proc. Int. Radar Conf. (RADAR)*, Oct. 2024, pp. 1–6.
- [19] H. Luo, Z. Zhu, M. Jiang, S. Guo, and G. Cui, "An effective multipath ghost recognition method for sparse MIMO radar," *IEEE Trans. Geosci. Remote Sens.*, vol. 61, 2023, Art. no. 5111611.
- [20] J.-K. Park, J.-H. Park, and K.-T. Kim, "Multipath signal mitigation for indoor localization based on MIMO FMCW radar system," *IEEE Internet Things J.*, vol. 11, no. 2, pp. 2618–2629, Jan. 2024.
- [21] W. Xie, F. Wen, J. Liu, and Q. Wan, "Source association, DOA, and fading coefficients estimation for multipath signals," *IEEE Trans. Signal Process.*, vol. 65, no. 11, pp. 2773–2786, Jun. 2017.
- [22] X. Hu, Y. Li, M. Lu, Y. Wang, and X. Yang, "A multi-carrier-frequency random-transmission chirp sequence for TDM MIMO automotive radar," *IEEE Trans. Veh. Technol.*, vol. 68, no. 4, pp. 3672–3685, Apr. 2019.
- [23] S. Sun, A. P. Petropulu, and H. V. Poor, "MIMO radar for advanced driver-assistance systems and autonomous driving: Advantages and challenges," *IEEE Signal Process. Mag.*, vol. 37, no. 4, pp. 98–117, Jul. 2020.
- [24] Y. Zhang et al., "3-D motion imaging in a multipath coordinate space based on a TDM-MIMO radar sensor," *IEEE Trans. Microw. Theory Techn.*, vol. 68, no. 11, pp. 4642–4651, Nov. 2020.
- [25] J. Capon, "High-resolution frequency-wavenumber spectrum analysis," *Proc. IEEE*, vol. 57, no. 8, pp. 1408–1418, 1969.
- [26] 77GHz mmWave Sensor EVMs. Accessed: Dec. 2021. [Online]. Available: <https://www.ti.com/lit/ds/swrs188d/swrs188d.pdfmymargin>
- [27] AWR2243 Evaluation Module. Accessed: Feb. 2021. [Online]. Available: <https://www.ti.com/lit/ug/spruit8d/spruit8d>
- [28] F. Adib, C.-Y. Hsu, H. Mao, D. Katabi, and F. Durand, "Capturing the human figure through a wall," *ACM Trans. Graph.*, vol. 34, no. 6, pp. 1–13, Nov. 2015.
- [29] S. Björklund, H. Petersson, A. Nezirovic, M. B. Guldogan, and F. Gustafsson, "Millimeter-wave radar micro-Doppler signatures of human motion," in *Proc. 12th Int. Radar Symp. (IRS)*, Sep. 2011, pp. 167–174.



Haolan Luo (Student Member, IEEE) received the B.S. degree in electronic science and technology from Anhui University, Hefei, China, in 2018, and the Ph.D. degree in signal and information processing from the University of Electronic Science and Technology of China (UESTC), Chengdu, China, in 2023.

He is currently a Post-Doctoral Fellow with UESTC. His research interests include target detection in multipath scenario, array signal processing, and target tracking.



Wenqiang Wei received the B.S. degree from Qingdao University, Qingdao, China, in 2020. He is currently pursuing the Ph.D. degree with the School of Information and Communication Engineering, University of Electronic Science and Technology of China, Chengdu, China. His current research interests are in array signal processing, multiple input multiple output (MIMO) waveform design, and optimization algorithm.



Meiqiu Jiang (Graduate Student Member, IEEE) received the B.S. degree in communication engineering from the University of Electronic Science and Technology of China, Chengdu, China, in 2021, where she is currently pursuing the Ph.D. degree with the School of Information and Communication Engineering.

Her research focuses on mmWave radar sensing and radar-based tracking.



Jinghui Zhu received the B.S. degree in communication engineering from Changsha University of Science and Technology, Changsha, China, in 2006, and the M.S. degree in communication engineering from Xidian University, Xi'an, China, in 2011.

She has been with the Television Science Research Institute, Beijing, China, since 2011. Her main research interests include radio and television frequency planning, wireless network planning and optimization, and converged media broadcasting.



Tong Gan received the B.S. degree in communication engineering from Xidian University, Xi'an, China, in 2009, the M.S. degree in signal and information processing from the Graduate University of Chinese Academy of Sciences, Beijing, China, in 2012, and the Ph.D. degree in signal and information processing from Kyoto University, Kyoto, China, in 2015.

Since 2016, he has been primarily engaged in engineering work related to digital signal processing for communication and radar equipment. In recent years, he has been conducting research in fields such as auto modulation recognition and autonomous information distribution, and leveraging AI as a core tool.



Shisheng Guo (Senior Member, IEEE) received the B.S. degree in communication engineering from Nanchang Hangkong University, Nanchang, China, in 2013, and the Ph.D. degree in signal and information processing from the University of Electronic Science and Technology of China (UESTC), Chengdu, China, in 2019.

He is currently a Researcher Fellow with the School of Information and Communication Engineering, UESTC and TianFu Jiangxi Laboratory, Chengdu, China. His research interests include through-the-wall radar imaging, signal analysis and non-line-ofsight target detection.



Guolong Cui (Senior Member, IEEE) received the B.S. degree in electronic information engineering, and the M.S. and Ph.D. degrees in signal and information processing from the University of Electronic Science and Technology of China (UESTC), Chengdu, China, in 2005, 2008, and 2012, respectively.

From January 2011 to April 2011, he was a Visiting Researcher with the University of Naples Federico II, Naples, Italy. From June 2012 to August 2013, he was a Post-Doctoral Researcher with the Department of Electrical and Computer Engineering, Stevens Institute of Technology, Hoboken, NJ, USA. From September 2013 to July 2018, he was an Associate Professor at UESTC, where since August 2018, he has been a Professor. His current research interests include cognitive radar, array signal processing, multiple input multiple output (MIMO) radar, and through-the-wall radar.